DOI: 10.4274/jems.2025.93206

Journal of ETA Maritime Science 2025;13(2):81-89

Investigation of the Hydrodynamic Characteristics of Tirhandil Boats with CFD Methods

Sertaç Bulut

İzmir Katip Çelebi University Faculty of Naval Architecture and Maritime, Department of Naval Architecture and Marine Engineering, Division of Ship Hydromechanics, İzmir, Türkiye

Abstract

Tirhandils, with their unique designs, have been used for various purposes in the Aegean and Mediterranean regions over centuries, becoming a significant part of our maritime culture. This study aims to investigate the hydrodynamic characteristics of Tirhandil boats using computational fluid dynamics methods. The objectives include analyzing resistance characteristics, pressure and velocity distributions, and wave patterns of a Tirhandil model with a waterline length of 12 meters and a waterline width of 4.02 meters at various flow speeds, corresponding to Froude numbers of 0.19, 0.28, 0.38, and 0.47. A grid independence study was conducted using various grid structures to determine the optimal mesh configuration for the numerical analyses. Validation studies were performed to evaluate the accuracy of the numerical models by comparing the numerical results with experimental data at a Froude number of 0.38, corresponding to a flow speed of 8 knots. Shear Stress Transport *k*-Omega and Realizable two-layer *k*-Epsilon turbulence models were used in the validation studies. The results indicate that frictional resistance dominates at lower speeds, notably at Froude number 0.19, while pressure resistance becomes the prevailing component at higher speeds, such as Froude numbers 0.38 and 0.47, with a balanced contribution observed at Froude number 0.28. A 2-knot increase in speed, results in an average increase of approximately 150% in total resistance. The highest-pressure areas on the hull are concentrated along the keel line at all flow speeds, with a more uniform pressure distribution observed at Froude number 0.38. As the flow speed increases, reaching a Froude number of 0.47, the pressure area in the bow region expands, leading to higher wave amplitudes, stronger stern waves, and significant increases in drag and resistance.

Keywords: Tirhandil, Hydrodynamics, Computational fluid dynamics, Resistance, Wave patterns

1. Introduction

Tirhandils are among the traditional and unique sailing boats specific to the Aegean and Mediterranean regions, characterized by their rich historical backgrounds, aesthetic forms, and resilience in challenging weather conditions. They are defined as one of the oldest known boat forms specific to the Aegean, distinguished by a hull form where the fore structure resembles the aft structure. The term "Tirhandil" is described as a type of sailing boat featuring a similar fore-aft design and a beak sail in the maritime dictionary Kamus-i Bahri Deniz Sözlüğü compiled by Nutki [1]. Tirhandil boats, with their short keel and wide hull design, have found extensive use in the fishing and sponge diving industries of Greece, Italy, and Türkiye [2]. The term "Tirhandil" in Greek originates from the word "trea-kena", meaning "one-third". The term "Tirhandil" in relation to the boats has been used to symbolize a one-third width-to-length ratio [3]. Developed over centuries of use in the Aegean and Mediterranean regions, the key features of Tirhandil boats include an overall boat length roughly three times the boat's width, a keel length approximately twice the boat's width, a symmetrical bow-stern profile, and masts equipped with reverse bow-stern rigging [3,4]. The symmetrical fore and aft form of Tirhandil boats, along with their inverted posts, further streamlines flow, reducing turbulence and enhancing efficiency. These design features, combined with their operational profile, make them uniquely suited for their traditional roles in the Mediterranean.

Address for Correspondence: Sertaç Bulut, İzmir Katip Çelebi University Faculty of Naval Architecture and Maritime, Department of Naval Architecture and Marine Engineering, Division of Ship Hydromechanics, İzmir, Türkiye
E-mail: sertac.bulut@ikcu.edu.tr
ORCID iD: orcid.org/0000-0002-4994-8148

Received: 30.08.2024
Last Revision Received: 30.01.2025
Accepted: 04.04.2025
Epub: 23.05.2025

To cite this article: S. Bulut, "Investigation of the hydrodynamic characteristics of Tirhandil boats with CFD methods." *Journal of ETA Maritime Science*, vol. 13(2), pp. 81-89, 2025.

The historical roots of Tirhandil boats, which date back to ancient times, including the Phoenicians [3], have their earliest documented records attributed to the year 1658 by G. D. Kriezis [5]. According to historian Dentes, the first Tirhandil boats were constructed in the 17th century on the island of Hydra [5]. Tirhandil boats have been used not only for fishing, and sponge diving, throughout their history but also for military purposes. In the Ottoman navy of 1790, which consisted of 90 vessels; it was determined that there were 20 Tirhandil boats [6]. It is stated that in 1831, nearly all traditional Ottoman-flagged ships were lateen-rigged vessels. In 1840, the majority of lateen-rigged Tirhandil boats were constructed in regions near İstanbul [7]. It is mentioned that lateen-rigged Tirhandil boats, with lengths ranging from 8 to 10 meters, were smaller vessels with lower carrying capacities. After 1849, lateen-rigged Tirhandil boats were replaced by larger vessels with an average carrying capacity 15 times greater, known as square-rigged (brig) Tirhandils [7]. In the 1950s, Tirhandil boats began to be produced in the Bodrum region of our country, and by the 1960s, they had also found their place in the waters of İstanbul [3]. Tirhandil boats produced within the Bodrum region were primarily used in sponge diving. In the beginning, they were operated by lateen sails and oars, but later, Bermuda-type sails took their place [2]. Their encounter with engines, however, took place only in the 1970s [3]. Tirhandil boats are also used for private and tourism purposes along the coasts of the Aegean and Mediterranean. In this regard, Tirhandil boats have found their place among the vessels in widespread use, thanks to the impact of sea tourism [8]. Figure 1 displays a Tirhandil-type boat located in the Bodrum region.

This study aims to investigate the hydrodynamic characteristics of Tirhandil boats using computational fluid dynamics (CFD) methods. The objectives of the study include evaluating the resistance characteristics, pressure and velocity distributions, and wave patterns of a Tirhandil model at Froude numbers of 0.19, 0.28, 0.38, and 0.47. A Tirhandil form, having a waterline length (L_{WL}) of 12 meters and a waterline width (B_{WL}) of 4.02 meters, was considered for the hydrodynamic analysis. The Tirhandil hull form was generated by computer-aided design systems. A grid independence study was conducted by employing various grid structures to determine the most appropriate mesh for the numerical analyses. The precision of the numerical results was evaluated through validation studies. Realizable two-layer *k*-Epsilon and Shear Stress Transport (SST) *k*-Omega models were selected to simulate turbulence structures for the validation studies. Numerical results were compared with experimental data [10] at the flow speed of 8 knots, corresponding to the Froude number of 0.38. The validation studies revealed that the numerical model closely matched the experimental results. It can be seen that the friction component dominates total resistance at 4 knots; friction and pressure components are in balance at 6 knots; and the pressure component becomes dominant at 8 knots and 10 knots. The highest wave amplitudes occur in the bow region of the full form, and, as the flow speed increases, the shoulder and stern waves become stronger. A review of existing literature shows that no previous study has presented such an elaborate analysis of the hydrodynamic design characteristics of Tirhandil boats. This study is a pioneering work in understanding the general design features and boat characteristics of Tirhandil boats, and it also provides a framework to guide potential hull form optimization efforts on the existing design.

Figure 1. *A traditional Tirhandil boat from Bodrum [9]*

2. Numerical Procedure

This section consists of two main parts, namely turbulence modelling and numerical setup. The turbulence-modelling part provides information on the governing equations and turbulence models used in numerical analyses to simulate the flow structures and turbulence distribution. The numerical setup part presents details on the physical models, mesh configuration, and computational domain.

2.1. Turbulence Modelling

The flow around the ship hull is effectively modeled by numerically solving the fundamental equations, including the continuity equation and the Navier-Stokes equations. In numerical computations, the URANS solver is applied, and the Navier-Stokes equations are discretized using the finite volume method. In CFD analyses, the Realizable two-layer *k*-Epsilon and SST *k*-Omega approaches are used to model the turbulent flow patterns around the hull form.

The continuity and Navier-Stokes equations are used as governing equations to evaluate the flow problems in this study. The continuity and momentum equations in Cartesian coordinates are presented in Equations (1) and (2).

$$\frac{\partial \rho}{\partial t} + \frac{\partial (\rho u_i)}{\partial x_i} = 0 \quad (1)$$

$$\rho\left(\frac{\partial u_i}{\partial t} + u_j \frac{\partial u_i}{\partial x_j}\right) = -\frac{\partial P}{\partial x_i} + \mu \frac{\partial^2 u_i}{\partial x_j^2} + f_i \quad (2)$$

where ρ presents the fluid density, $u\ i$ denotes the velocity component, P refers to the pressure field, μ symbolizes the dynamic viscosity, and f_i is the external force.

RANS models, including the Realizable two-layer *k*-Epsilon [11] and SST *k*-Omega [12] models, are employed to simulate flow structures and turbulence distribution. Filtering and Reynolds averaging approaches are commonly used to convert Navier-Stokes equations into a solvable form, without directly simulating the turbulent structures at small scales. The Reynolds averaging approach evaluates a flow variable by decomposing it into a mean component $\overline{\theta}(x,t)$ and a fluctuating component $\theta'(x,t)$ (Equation 3).

$$\theta(x,t) = \overline{\theta}(x,t) + \theta'(x,t) \quad (3)$$

Equation (4) presents the RANS equations, obtained from the incompressible form of the Navier-Stokes equations.

$$\frac{\partial}{\partial t}(\rho \overline{u}_i) + \frac{\partial}{\partial x_j}(\rho \overline{u}_i \overline{u}_j) = -\frac{\partial \overline{p}}{\partial x_i} + \frac{\partial}{\partial x_j}\left[\mu\left(\frac{\partial \overline{u}_i}{\partial x_j} + \frac{\partial \overline{u}_j}{\partial x_i}\right)\right] + \frac{\partial R_{ij}}{\partial x_j} \quad (4)$$

where $\overline{u}_i$ and $\overline{u}_j$ presents Reynolds-averaged velocities and $\overline{p}$ denotes the Reynolds-averaged pressure. The main difference between the Navier-Stokes and RANS equations is the addition of the Reynolds stress tensor R_{ij}, described according to the Boussinesq hypothesis [13] in Equation 5.

$$R_{ij} = -\rho \overline{u_i u_j} = \mu_t\left(\frac{\partial \overline{u}_i}{\partial x_j} + \frac{\partial \overline{u}_j}{\partial x_i}\right) - \frac{2}{3} k \delta_{ij} \quad (5)$$

The *k*-Epsilon and *k*-Omega turbulence models, which are derived from the Boussinesq hypothesis, determine eddy (turbulent) viscosity μ_t using distinct techniques. μ_t Turbulent viscosity, as expressed in Equation (6), is determined by the *k*-Epsilon model [11,14], through the use of turbulent kinetic energy (k) and turbulence dissipation rate (ε).

$$\mu_t = \rho C_\mu \frac{k^2}{\varepsilon} \quad (6)$$

where C_μ is a model constant. The realizable approach, and two-layer technique are combined under the framework of the realizable two-layer k-epsilon model. The two-layer technique solves k (turbulent kinetic energy) throughout the entire flow field, while ε (turbulent dissipation rate) and μ_t (eddy viscosity) are modeled based on their dependence on wall distance in the layer near the wall. By applying the realizable approach, mathematical constraints related to normal stresses can be imposed to align with turbulence characteristics. Turbulent viscosity is determined in the k-Omega model [15] through the use of turbulent kinetic energy (k) and the specific dissipation rate (ω), as expressed in Equation (7).

$$\mu_t = \alpha^* \frac{\rho k}{\omega} \quad (7)$$

The SST variant of the *k*-Omega model merges the standard *k*-Omega model for near-wall regions and the standard k-Epsilon model for the far-field using a blending function. This model also incorporates a new method for eddy viscosity, taking into consideration the transport of principal turbulent shear stress.

2.2. Numerical Setup

An overview of the numerical setup for all simulations is provided in this section. The realizable two-layer *k*-Epsilon and SST *k*-Omega models are employed in CFD analyses to simulate the turbulent flow structures around the hull form. In the numerical simulations, a segregated flow solver is applied to solve each momentum equation sequentially, utilizing an algebraic multigrid method. The governing transport equations are spatially discretized with an upwind scheme of second order for both convection and diffusion terms. A first-order implicit unsteady scheme is used to discretize the temporal terms in the governing equations. The simulations use a constant time-step of 0.004 seconds and 10 inner iterations, as recommended by ITTC's procedure for Reynolds stress turbulence models and shown in Equation 8 [16]. Multiphase flow modeling is used to simulate a floating boat at the free water surface. Free surface effects are represented by using the volume of fluid approach, which involves tracking the interface between two or more immiscible fluid phases.

$$\Delta t = 0.001 \sim 0.0025\ L/U \quad (8)$$

The accuracy of fluid flow simulations and the solution convergence rate are directly affected by the mesh construction process. Particular focus on mesh quality is given to specific regions within the computational domain. The domain is locally refined through the application of mesh refinement volumes. Local mesh refinements are concentrated near the hull form, bow, stern, free surface, and wake field. The use of the trimmed cell mesher technique provides robust and efficient mesh structuring. According to recommendations from the ITTC guide [16,17] 10 prism layers with a 1.2 expansion ratio are employed. Grid independence analysis is carried out to determine the optimal grid structure for numerical analyses. A smooth transition between the prism layers and the outer volume mesh is achieved through specific refinement regions. Figure 2 shows that the computational domain includes approximately 1.7 million cells.

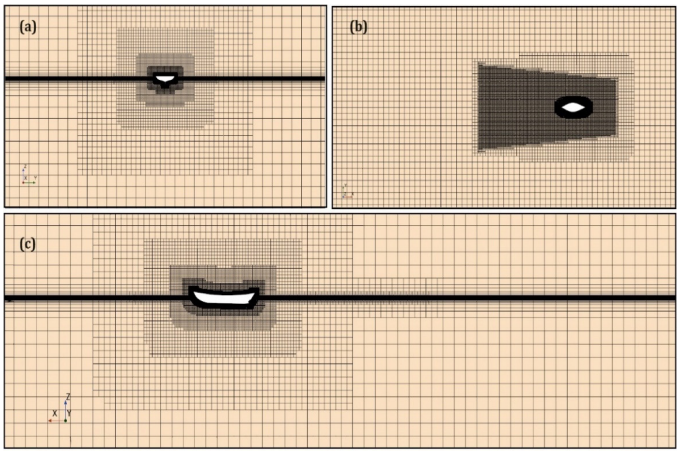

Figure 2. *Body front (a), top (b), and side (c) views of the mesh structure*

Achieving accurate solutions significantly depends on the proper positioning of domain boundaries and the selection of boundary conditions. Domain boundaries are placed approximately 3 length overall (L_{OA}) from the bow, 8 L_{OA} downstream of the stern, 3 L_{OA} from the symmetry plane on the sides, 2 L_{OA} below the keel, and 1 L_{OA} above the deck. The computational domain setup follows the recommendations provided by ITTC guidelines [16,17]. The boundary conditions for the numerical simulations are defined as follows: symmetry planes for the side boundaries; pressure outlet at the outlet surface behind the ship hull; non-slip wall on the boat surface; and velocity inlet at the inlet, top, and bottom surfaces of the computational domain. The computational domain and the corresponding boundary conditions are presented in Figure 3. Accurate results are provided with All y+ wall treatment by applying y+ ≈ 30 in the SST *k*-Omega model (Figure 4), which effectively resolved the buffer and inertial sublayers, and y+ ≈ 70 in the realizable Two-Layer variant of *k*-Epsilon model, targeting the inertial sublayer.

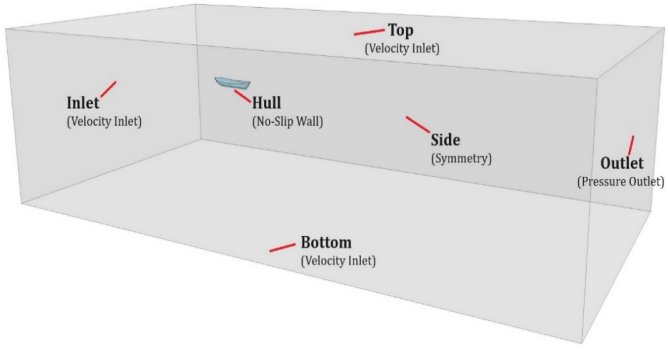

Figure 3. *Overview of the computational domain and boundary conditions*

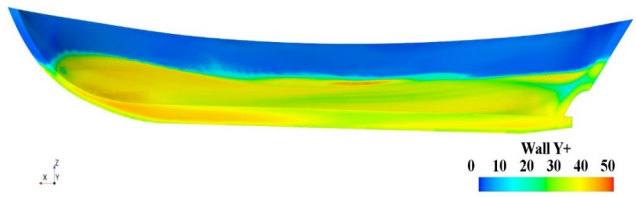

Figure 4. *Wall Y+ distribution along the hull of the Tirhandil boat at Fn=0.47*

3. Results

The results are presented in two main parts. In the first part, grid independence studies are conducted to determine the most appropriate mesh configuration for numerical simulations, and the numerical model is validated with experimental results. In the second part, the hydrodynamic characteristics of the Tirhandil form at various flow velocities were investigated by using CFD methods.

3.1. Model Validation and Grid Independence Study

Accurate modeling of the boundary layer and fulfilling turbulence model requirements are important for the precision of numerical analysis. An appropriate mesh setup provides an effective trade-off between computational costs and accuracy. The grid convergence index (GCI) method is used to estimate discretization errors, resulting in the generation of the optimal mesh configuration [18]. The computed GCI parameters for the Tirhandil model at a Froude number (Fn) of 0.38 for the coarse, medium, and fine meshes, with 1.2 million, 1.7 million, and 2.4 million cells, respectively, are presented in Table 1. The total resistance coefficient (C_T) is used as the benchmark parameter to assess mesh discretization errors. The grid refinement factor, r, is defined as the ratio of the grid size in the finer mesh to the

Table 1. *Grid convergence calculations for the reference model (RF)*

Parameters	Fn=0.38
$N_1, N_2, N_3 (x10^{-6})$	2.4, 1.7, 1.2
G1, G2, $G_3 (x10^3)$	8.409, 8.575, 9.271
φ^{21}_{ext}	0.84
e^{21}_{a} (%)	1.97
e^{21}_{ext} (%)	0.62
GCI^{21}_{fine} (%)	0.77
GCI^{32}_{med} (%)	3.18

grid size in the coarser mesh. The apparent order of accuracy is determined according to the definitions in Equations (9-11).

$$p = \frac{1}{\ln(r_{21})}\left|\ln\left|\varepsilon_{32}/\varepsilon_{21}\right| + q(p)\right| \quad (9)$$

$$q(p) = \ln\left(\frac{r_{21}^{p} - s}{r_{32}^{p} - s}\right) \quad (10)$$

$$s = 1 \times sgn\left(\varepsilon_{32}/\varepsilon_{21}\right) \quad (11)$$

where, ε_{32} is defined as $\theta_3 - \theta_2$ and ε_{21} as $\theta_2 - \theta_1$, with θ_k representing the solution on the kth grid. The presence of negative values of $\varepsilon_{32}/\varepsilon_{21}$ <0 indicates oscillatory convergence [18]. The extrapolated values are obtained using Equation (12).

$$\theta_{ext}^{21} = \left(r_{21}^{p}\theta_1 - \theta_2\right)/\left(r_{21}^{p} - 1\right) \quad (12)$$

θ_{ext}^{32} can be computed in a similar way. Equations (13, 14) are used to determine the extrapolated relative error $\left(e_{ext}^{21}\right)$ and estimated relative error $\left(e_{a}^{21}\right)$.

$$e_{a}^{21} = \left|\frac{\theta_1 - \theta_2}{\theta_1}\right| \quad (13)$$

$$e_{ext}^{21} = \left|\frac{\theta_{ext}^{12} - \theta_1}{\theta_{ext}^{12}}\right| \quad (14)$$

The GCI between the fine and medium grids is determined using Equation (15).

$$GCI_{fine}^{21} = \frac{1.25 \cdot e_{a}^{21}}{r_{21}^{2} - 1} \quad (15)$$

Considering the total resistance (R_T) shows that each mesh refinement contributes to a decrease in GCI $\left(GCI_{fine}^{21} < GCI_{med}^{32}\right)$. The decrease in GCI between the coarser mesh and the finer mesh is notably high, as shown in Table 1. The results imply that the solution is nearly grid-independent, and further refinement is expected to result in minimal changes to the results. Consequently, the medium grid containing 1.7 million cells was chosen for CFD analyses, considering both computational cost and accuracy.

Validation of the CFD analysis concerning the Tirhandil model's hydrodynamic characteristics was achieved through a comparison with experimental results from the literature. The validation studies employed results from model tests on Tirhandil forms, performed by Ganos and Loukakis [10]. The validation studies were performed at a Froude number of 0.38. The CFD analyses employed the realizable two-layer *k*-Epsilon and SST *k*-Omega turbulence models. The total resistance of the form was considered in a comparison between the CFD analysis results and experimental data. The total resistance is represented in dimensionless form as the Froude resistance coefficient (C_{Fn}), as defined in Equations (16, 17).

$$C_{Fn} = \frac{1000.R_T.M^2}{(4.\pi.\rho.g).Fn^2.L^3} \quad (16)$$

$$M = \frac{L}{\nabla^3} \quad (17)$$

where ρ refers to the seawater density, g is the acceleration of gravity, ∇ represents the ship volume of displacement, R_T signifies the total resistance, L represents the L_{WL}, and Fn indicates the Froude number. The general dimensions of the Tirhandil form, designed based on the test model used in the experiments, are presented in Table 2. The body plan and perspective view of the Tirhandil model are shown in Figure 5.

Table 3 provides a comparison of total resistance values at a Froude number of 0.38 from CFD analyses using the realizable two-layer *k*-Epsilon and SST *k*-Omega turbulence models against experimental results [10]. The results indicate that the SST *k*-Omega turbulence model has a good agreement with experimental results, with a difference of 4.68%, while the realizable two-layer *k*-Epsilon model shows a significant difference of 14.41% compared to experimental data. The validation studies confirmed that the SST *k*-Omega turbulence model provided results that closely match the

Table 2. *Specifications of the Tirhandil model*

Specifications	Tirhandil model
Displacement (tones)	10.58
Overall length (L_{OA}) (m)	13.66
Waterline length (L_{WL}) (m)	12.00
Waterline width (B_{WL}) (m)	4.02
Draft (m)	1.08

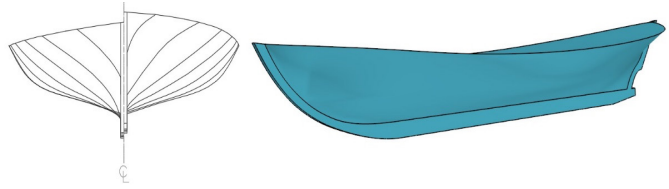

Figure 5. *Body plan and perspective view of the Tirhandil model*

Table 3. *Total resistance values obtained from RANS models and experiments*

	Experiment [10]	*k*-Omega	*k*-Epsilon
C_{Fn}	2.70	2.574	2.311
Difference (%)		4.68	14.41

experimental results. Consequently, the SST *k*-Omega turbulence model was employed in the CFD analyses to investigate the hydrodynamic characteristics of the Tirhandil model at various flow velocities.

3.2. Analysis on the Hydrodynamic Characteristics of the Tirhandil Model

This section presents a comprehensive evaluation of the hydrodynamic characteristics of the Tirhandil model using CFD methods. The CFD analyses include a detailed investigation of resistance characteristics, velocity distribution, and wave patterns. Numerical simulations were conducted using the commercial STAR-CCM+ software [19]. The optimization framework was implemented by two PC clusters, each equipped with 24 Intel Core (64-bit, 3.0 GHz up to 5.8 GHz) processors, which were acquired with funding provided by the Technological Research Council of Türkiye (TUBITAK).

Figure 6 presents the variation in resistance characteristics of the Tirhandil model according to changes in flow velocity. In CFD analyses, the total resistance of the ship is considered a combination of pressure resistance and friction resistance components. Pressure resistance results from pressure forces acting perpendicularly to the ship's surface, encompassing wave-making resistance and other pressure-induced forces. Friction resistance is caused by viscous forces between a ship's hull and the surrounding water, generating shear stress on the hull's surface and leading to energy loss. It is revealed that at a flow speed of 4 knots (Fn=0.19), the friction components are dominant in the total resistance, while, at 6 knots (Fn=0.28), the pressure and friction components are in balance. At flow speeds of 8 knots (Fn=0.38) and 10 knots (Fn=0.47), the pressure components become more dominant in the total resistance. At the characteristic cruising speed of 8 knots for Tirhandils, the total resistance is approximately 2.2 kN, with 64.8% of this resistance attributed to pressure components and 35.2% to friction components. When the cruising speed increases to 10 knots, the total resistance reaches approximately 5.7 kN, with pressure components accounting for 76.9% of the total resistance. At low speeds, shear effects dominate, making the friction component the main part of total resistance. As flow speeds increase, the pressure component becomes more dominant due to the generation of internal waves, higher dynamic pressure at the bow, and increased wave interactions along the hull [20-22]. At cruising speeds of 4 knots and 6 knots, the total resistance is approximately 0.3 kN and 0.8 kN, respectively. It can be seen that a 2-knot increase within the evaluated cruising speed range, leads to an average increase of approximately 150% in total resistance.

Figure 7 shows the total pressure distribution on the Tirhandil hull form for the flow speeds of 6 knots, 8 knots, and 10 knots. The pressure for all cruising speeds are concentrated along the keel, and as the flow speed increases, the high-pressure area extends towards the front of the keel. At a speed of 6 knots, the pressure area under the hull is broader, as with increasing speed, this area gradually narrows.

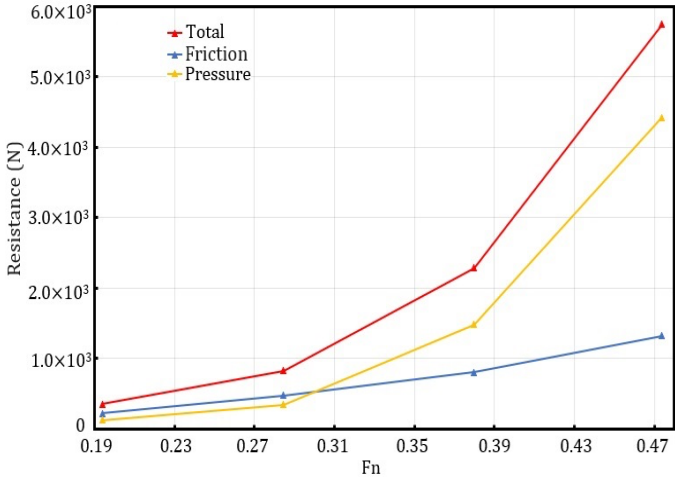

Figure 6. *Total resistance and resistance components of Tirhandil model at various cruising speeds*

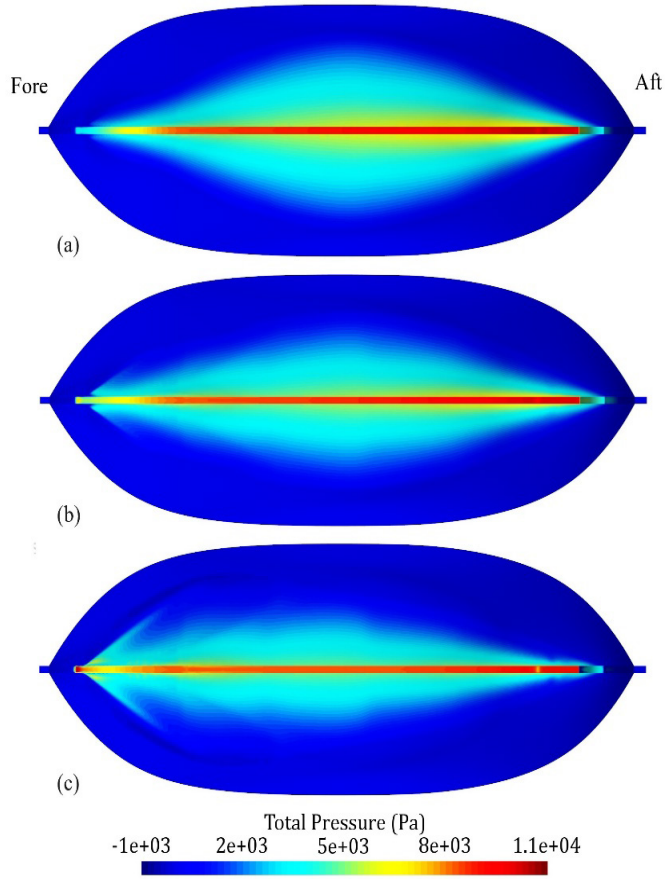

Figure 7. *Total pressure distribution of Tirhandil model at 6 knots (a), 8 knots (b), and 10 knots (c)*

At the characteristic cruising speed of 8 knots, the pressure distribution under the hull becomes more uniform. As the flow speed reaches 10 knots, the pressure area in the bow region expands. In this situation, the wave amplitudes at the bow region increase, contributing to additional resistance.

Figure 8 presents the wave patterns around the Tirhandil model at flow speeds of 6 knots, 8 knots, and 10 knots. The wave amplitudes around the hull form at a flow speed of 6 knots are lower than those at higher speeds. The highest wave amplitudes are observed at the bow of the hull. At a flow speed of 6 knots, the maximum wave amplitude at the bow is 0.29 m, rising to 0.46 m at 8 knots and 0.63 m at 10 knots. The wave distribution around the hull form at 8 knots is more regular and less pronounced compared to 10 knots, indicating a reduction in turbulence and smoother flow separation. At 10 knots, stronger shoulder and stern waves are generated, resulting in higher wave resistance, diminished flow stability, and reduced overall hydrodynamic efficiency [23-25].

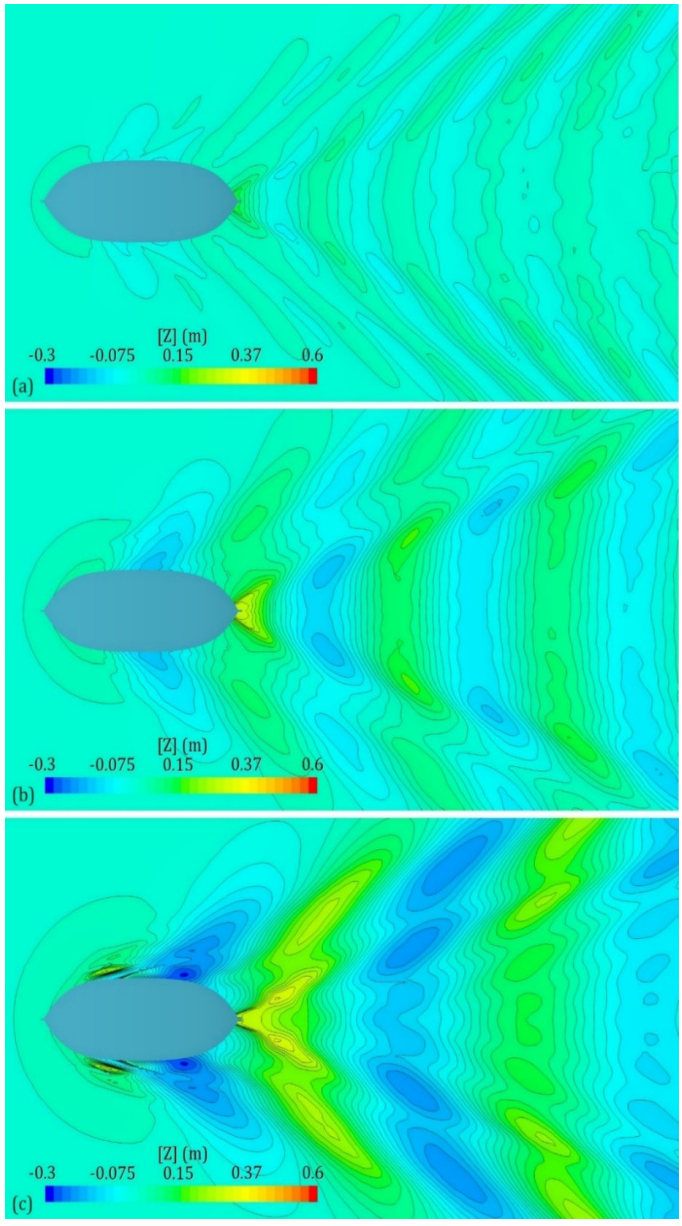

Figure 8. *Wave patterns around Tirhandil model at 6 knots (a), 8 knots (b), and 10 knots (c)*

Figure 9 illustrates the velocity distribution around the hull form at flow speeds of 6 knots, 8 knots, and 10 knots. The velocity distribution is presented in a dimensionless form, normalized by the free-stream velocity. As the flow speed increases, there are significant changes in the velocity distributions, particularly around the bow and stern regions. As the flow speed increases from 6 knots to 8 knots and 10 knots, the low-velocity regions in the bow and stern areas become progressively stronger and larger. Such low-velocity regions generally result in significant pressure differences, negatively impacting resistance and potentially increasing drag [24,25]. A more balanced velocity distribution contributes to the resistance characteristics and the formation and propagation of waves.

4. Conclusion

In this study, the hydrodynamic characteristics of Tirhandil boats were evaluated at various cruising speeds using CFD methods. The Tirhandil model considered in the hydrodynamic analyses has a L_{WL} of 12 meters and a B_{WL} of 4.02 meters. The resistance characteristics, pressure and velocity distributions, and wave patterns of the Tirhandil

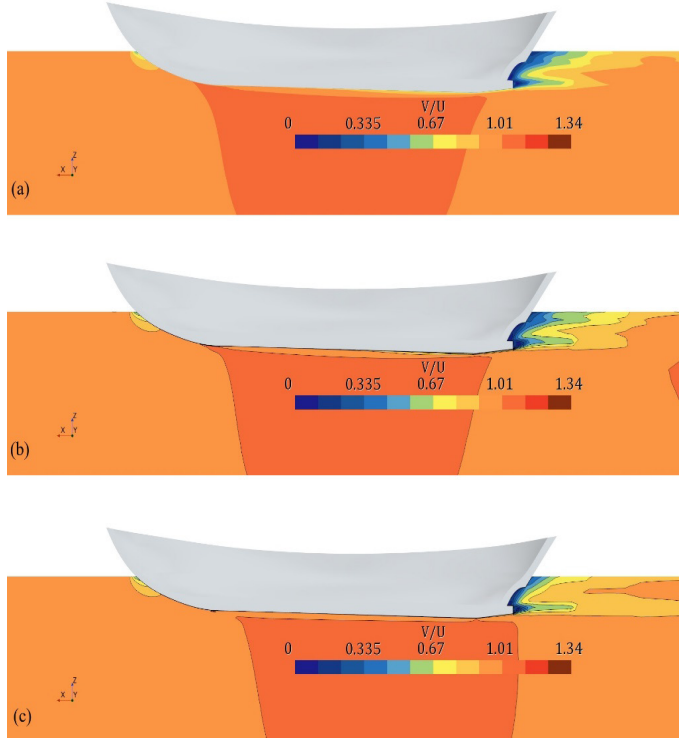

Figure 9. *Velocity distribution of Tirhandil model at 6 knots (a), 8 knots (b), and 10 knots (c)*

form were evaluated by performing CFD analysis at flow speeds corresponding to Froude numbers of 0.19, 0.28, 0.38, and 0.47. The appropriate mesh configuration for the numerical analyses was determined by conducting a grid independence study using different grid structures. Validation studies were performed to evaluate the accuracy of the flow analyses by comparing the numerical models with experimental results [10] at a Froude number of 0.38. SST *k*-Omega and Realizable Two-Layer *k*-Epsilon were used as turbulence models in the validation studies. The validation studies revealed that the numerical results were in good agreement with the experimental data.

There have been significant changes in resistance characteristics with the increase in cruising speed. It has been noted that friction components dominate the total resistance at a flow speed of 4 knots, while pressure components prevail at 8 and 10 knots. At 6 knots, there is a balanced distribution among these components. It is also revealed that a 2-knot increase within the evaluated cruising speed range, results in an average increase of approximately 150% in total resistance. The highest-pressure areas on the hull form are observed along the keel line across the entire range of cruising speeds. At 8 knots, the pressure distribution under the hull becomes more uniform. As the flow speed increases to 10 knots, the pressure area at the bow region expands, resulting in higher wave amplitudes and increased resistance. Higher amplitude waves are observed around the hull form as the flow speed increases. The highest amplitude waves occur at bow region for all cruising speeds. Compared to 10 knots, the wave distribution around the hull form at 8 knots is more regular and less pronounced, indicating smoother flow and reduced turbulence. At 10 knots, stronger shoulder and stern waves generate higher wave resistance and diminish flow stability. As the flow speed increases, the low-velocity areas in the bow and stern regions broaden and strengthen, resulting in significant pressure differences that negatively impact resistance and potentially increase drag.

This study is a pioneering work that presents a comprehensive investigation of the hydrodynamic design characteristics of Tirhandil boats. It also provides a framework to guide future research related to Tirhandils in the fields of hydrodynamics and hull form optimization. In the future, similar studies could be expanded by considering harsh water conditions, and the performance of different turbulence models could also be evaluated.

Footnotes

Fundings: *This research is supported by the Scientific and Technological Research Council of Türkiye (TUBITAK) under Project Number 223M093 within the framework of the project titled "Determination of Design Criteria and Form Optimization for Turkish Type Tirhandil Boats".

*This research is supported by İzmir Katip Çelebi University Scientific Research Projects Commission (BAP) under Project Number 2024-GAP-GİDF-0010 within the framework of the project titled "Green Transition in Blue Voyage: Eco-Friendly Tırhandil Design with Fuel Cell Technology".

References

[1] S. Nutki, *Kamus-i Bahri-Deniz Sözlüğü*, İstanbul: Türkiye İş Bankası Kültür Press, 2011.

[2] S. Özen, *Gemiler Sözlüğü*, İstanbul: Denizler Publishing, 2017

[3] Y. Köyağasıoğlu, *Denizin Kanatlı Perileri Yelkenliler*, İstanbul: Naviga Publishing, 2014.

[4] K. Damianidis, "Vernacular boats and boatbuilding in Greece", Ph.D. dissertation, University of St. Andrews, St Andrews, Scotland, 1991.

[5] M. C. Gür, *Kürekten Yelkene Kaybolan Miras*, İstanbul: Koç University Press, 2020.

[6] A. I. Gencer, *Bahriye'de Yapılan Islahat Hareketleri ve Bahriye Nezareti'nin Kuruluşu (1789 - 1867)*, Ankara: Turkish Historical Society Publications, 2001.

[7] E. Mahmuzlu, "Ottoman-flagged ships, 1830s-1860s: hull, rig, and geography", *Drassana: revista del Museu Marítim*, vol. 27, pp. 120-168, Dec 2019.

[8] B. I. Turan, and M. Akman, "Modeling and comparison of Bodrum gulets' hull forms with round and transom", *Journal of ETA Maritime Science*, vol. 9, pp. 120-129, Apr 2021.

[9] Bodrum Time, "*Tirhandil Cup'da Heyecanli Gümüşlük Rotası*", March 20, 2020. [Online]. Available: https://www.bodrumtime.net/2020/03/12/tirhandil-cupda-heyecanli-gumusluk-rotasi/ [Accessed: Aug 28, 2024].

[10] G. Ganos, and T. Loukakis, "*Resistance characteristics of the trehantiri type boat*", report of research group: ship hydromechanics and structures (Mechanical, maritime and materials engineering), Delft University of Technology, Netherlands, 1986.

[11] W. P. Jones, and B. E. Launder, "The prediction of laminarization with a two-equation model of turbulence", *International Journal of Heat and Mass Transfer,* vol. 15, pp. 301-314, Feb 1972.

[12] F. R. Menter, "Two-equation eddy-viscosity turbulence models for engineering applications", *AIAA Journal*, vol. 32, pp. 1598-1605, Aug 1994.

[13] J. Boussinesq, "Essai sur la theorie des eaux courantes", *Mémoires présentés par divers savants à l'Académie des Sciences,* vol. 13, pp. 1-680, 1877 [in French].

[14] B. E. Launder, and B. I. Sharma, "Application of the energy-dissipation model of turbulence to the calculation of flow near a spinning disc.", *Letters in Heat and Mass Transfer*, vol. 1, pp. 131-137, Dec 1974.

[15] D. C. Wilcox, "Reassessment of the scale-determining equation for advanced turbulence models", *AIAA Journal*, vol. 26, pp. 1299-1310, Nov 1988.

[16] ITTC, "*Practical guidelines for ship CFD applications-recommended procedures and guidelines*", in 26th ITTC Specialist Committee on CFD in Marine Hydrodynamics, 75-03-02-03, Sep 2011.

[17] ITTC, "*Final report and recommendations to the 27th ITTC*", in 27th ITTC Specialist Committee on CFD in Marine Hydrodynamics, Dec 2014. Available: https://ittc.info/media/6095/sc-renewables.pdf

[18] I. B. Celik, U. Ghia, P. J. Roache, and C. J. Freitas, "Procedure for estimation and reporting of uncertainty due to discretization in CFD applications", *Journal of Fluids Engineering-Transactions of the ASME*, vol. 130, 078001, Jan 2008.

[19] StarCCM+ version 2310, "*User guide*", SIEMENS Simcenter, 2023.

[20] S. Song, Y. K. Demirel, and M. Atlar, "An investigation into the effect of biofouling on the ship hydrodynamic characteristics using CFD", *Ocean Engineering*, vol. 175, pp. 122-137, Mar 2019.

[21] M. Terziev, T. Tezdogan, and A. Incecik, "A numerical assessment of the scale effects of a ship advancing through restricted waters", *Ocean Engineering*, vol. 229, 108972, Jun 2021.

[22] P. Reid, M. Terziev, T. Tezdogan, and A. Incecik, "The effect of flow stratification on ship performance: a numerical study", *Ships and Offshore Structures*, vol. 19, pp. 1827-1839, Feb 2024.

[23] T. Tezdogan, et al. "An investigation into fishing boat optimization using a hybrid algorithm", *Ocean Engineering*, vol. 167, pp. 204-220, Nov 2018.

[24] A. Nazemian, and P. Ghadimi, "Multi-objective optimization of ship hull modification based on resistance and wake field improvement: combination of adjoint solver and CAD-CFD-based approach", *Journal of the Brazilian Society of Mechanical Sciences and Engineering*, vol. 44, pp. 1-27, Dec 2021.

[25] A. Hamed, "Multi-objective optimization method of trimaran hull form for resistance reduction and propeller intake flow improvement", *Ocean Engineering*, vol. 244, 110352, Jan 2022.